

Demonstration of Quantum Advantage in Microwave Quantum Radar

R. Assouly,¹ R. Dassonneville,¹ T. Peronnin,¹ A. Bienfait,¹ and B. Huard^{1,*}

¹*Ecole Normale Supérieure de Lyon, CNRS, Laboratoire de Physique, F-69342 Lyon, France*

(Dated: November 11, 2022)

While quantum entanglement can enhance the performance of several technologies such as computing, sensing and cryptography, its widespread use is hindered by its sensitivity to noise and losses. Interestingly, even when entanglement has been destroyed [1–3], some tasks still exhibit a quantum advantage Q , defined by a Q -time speedup, over any classical strategies. A prominent example is the quantum radar [3], which enhances the detection of the presence of a target in noisy surroundings. To beat all classical strategies, Lloyd [3] proposed to use a probe initially entangled with an idler that can be recombined and measured with the reflected probe. Observing any quantum advantage requires exploiting the quantum correlations through a joint measurement of the probe and the idler [4]. In addition to successful demonstrations of such quantum illumination protocols at optical frequencies [5, 6], the proposal of a microwave radar [7], closer to conventional radars, gathered a lot of interest. However, current microwave implementations [8–14] have not demonstrated any quantum advantage as probe and idler were always measured independently [15–17]. In this work, we implement such a measurement using a superconducting circuit and demonstrate a quantum advantage $Q > 1$ for microwave radar. Storing the idler mitigates the detrimental impact of microwave loss on the quantum advantage, and the purity of the initial entangled state emerges as the next limit. While the experiment is a proof-of-principle performed inside a dilution refrigerator, it exhibits some of the inherent difficulties in implementing quantum radars such as the limited range of parameters where a quantum advantage can be observed or the requirement for very low probe and idler temperatures.

We focus on the simplest radar protocol, where the goal is to detect whether a target is present with a minimum number M of attempts. Each attempt corresponds to using a single microwave mode in time-frequency space to probe the target, with the constraint that the probe contains a fixed number N_S of signal photons on average (Fig 1a) and is detected in a background noise of N_N photons. We consider that all other parameters are known: target position, speed and reflectivity κ . Several metrics can quantify the performance

of a radar. We choose the error exponent defined as $\mathcal{E} = \lim_{M \rightarrow \infty} -\frac{1}{M} \log P_{\text{error}}(M)$. It gives the asymptotic scaling of the average error probability $P_{\text{error}}(M) \sim \text{poly}(M)e^{-\mathcal{E}M}$, where M the number of probe modes used and $\text{poly}(M)$ is a polynomial of M . For simplicity, we assume no prior knowledge on the target state: initially the target is present with a probability $\frac{1}{2}$. Under the assumptions of the central limit theorem, the number of required attempts to reach a given error probability scales as $1/\mathcal{E}$. The quantum advantage can thus be defined as $Q = \mathcal{E}/\mathcal{E}_{\text{cl}}$, where \mathcal{E}_{cl} is the error exponent of the best classical strategy.

Given a certain probe state, the largest achievable error exponent for any measurement apparatus is the so-called quantum Chernoff bound [18]. De Palma and Boregaard [19] showed that the best classical strategy (i.e. without quantum memory) is to use a coherent state as a probe, which gives an optimum $\mathcal{E}_{\text{cl}} = \frac{\kappa N_S}{4N_N}$. This limit is asymptotically reached by a homodyne measurement in the large noise ($N_N \gg 1$) limit [20]. Quantum strategies rely on initially entangling the probe with an idler [3]. The quantum Chernoff bound for quantum radar is $\mathcal{E}_{\text{max}} = \frac{\kappa N_S}{N_N}$ in the low signal $N_S \ll 1$, high noise $N_N \gg 1$ regime [19], which shows that the quantum advantage is at best $Q_{\text{max}} = 4$ for radars. Effectively, it can be reached using one mode of a two-mode squeezed vacuum state (TMSV) to illuminate the target [21, 22]. However, there is no known detector that can reach this advantage $Q_{\text{max}} = 4$ without a global joint measurements of M modes of all attempts [23, 24]. Using simpler pairwise joint measurements instead [20, 25, 26], it is nevertheless possible to reach $Q = 2$ with $\mathcal{E}_{\text{pair}} = \frac{\kappa N_S}{2N_N}$.

Here we implement this pairwise joint measurement using a superconducting circuit [27–29] that also generates the TMSV state [30–33], and stores the idler mode while the signal probe travels. We then experimentally determine the error exponent of this quantum radar for various signal and noise photon numbers. To ensure a fair determination of the experimental quantum advantage Q , the absolute best classical error exponent \mathcal{E}_{cl} must be determined. Previous microwave radar experiments managed to exceed the error exponent of one instance of classical radar [8–14], but could not break the classical upper bound \mathcal{E}_{cl} . A central challenge of the experiment thus consists in performing precise calibrations of the target and radar parameters κ , N_S and N_N .

Microwave Quantum Radar Implementation Our superconducting device contains two resonators called buffer and memory and operates at 15 mK (Fig. 1b). The buffer, which emits and receives the probe signal, has frequency $\omega_b/(2\pi) = 10.20$ GHz and is coupled to

* benjamin.huard@ens-lyon.fr

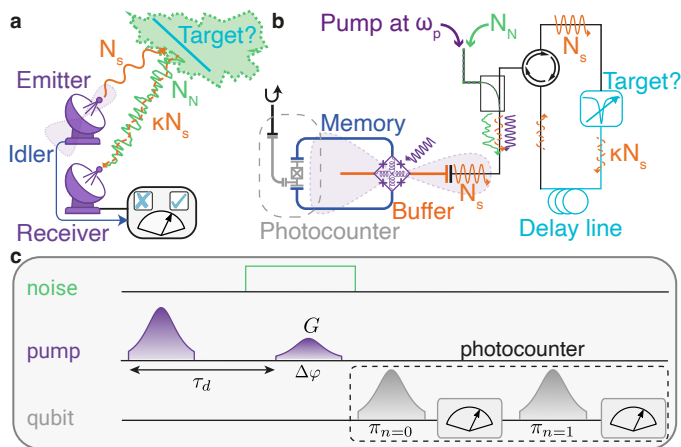


FIG. 1. Quantum radar principle and implementation. **a)** An emitter sends a signal mode with photon number N_S to determine the presence of a target using the least possible number of attempts. The signal is reflected or not from the target, with reflectivity κ , in a thermal environment with mean photon number N_N . A receiver processes all reflected signals and decides whether the target is present or not. Quantum probes can be initially entangled with an idler whose processing by the receiver leads to faster determination and thus a quantum advantage compared to any classical probe. The advantage crucially relies on the exploitation of quantum correlations by a joint measurement between idler and received signal. **b)** Superconducting circuit (left) probing a target composed of a delay line and tunable notch filter (right). It comprises a non-linear device (purple) generating and decoding entangled pairs between buffer mode (orange) and idler memory mode (blue). A transmon qubit (grey) completes the joint measurement. The entangling pump and thermal noise background are injected through a directional coupler into the buffer port. **c)** Pulse sequence of the quantum radar experiment. The phase difference $\Delta\varphi$ and delay τ_d between pump pulses, as well as the gain G of the second pump pulse can all be tuned to maximize the error exponent. The dashed box represents the observable measurement by the qubit on the memory for the quantum radar but can be replaced by other photocounting schemes for calibration purposes (see Supplementary Material).

a transmission line with rate $\gamma_b/(2\pi) = 25$ MHz. The memory, which stores the idler, has frequency $\omega_m/(2\pi) = 3.74617$ GHz and a decay rate of $\gamma_m/(2\pi) = 40$ kHz. The resonators are coupled by a Josephson Ring Modulator (JRM, purple in Fig. 1b) [34–36]. We apply a first pump tone at a frequency $\omega_p = \omega_b + \omega_m$ for 28 ns, generating a TMSV state between the memory and a probe mode immediately exiting the buffer [37] (see Fig. 1c). The probe propagates to the target and comes back when present, yet attenuated by a factor κ . The target is composed of a flux tunable notch filter (see Supplementary Material) followed by a 12-m-long coaxial cable, allowing to tune the target reflectivity in situ from maximum (target is present) to a value two orders of magnitude lower (target is absent). The reflected probe is then combined with thermal noise injected via a weakly coupled auxil-

ary line. The noise is generated at room temperature by amplifying the Johnson-Nyquist noise of a $50\ \Omega$ resistor with tunable gain (see Supplementary Material). A quantum advantage can only be observed for $N_N > 1$, yet the generation of the TMSV state requires the buffer to be as cold as possible. We thus only switch on the noise source after the TMSV state has been prepared and exited the buffer mode.

The joint measurement is finally performed as follows. We drive the JRM by a pump at ω_p . The resulting two-mode squeezing operation prepares a memory state that encodes the presence or absence of quantum correlations between probe and idler [20]. The proposal of Guha and Erkmén [20] recommends to measure the number of photons in the memory to reach up to $Q = 2$. Due to finite coherence times, we chose a different detector based on an ancillary transmon qubit dispersively coupled to the memory. Despite the large noise background, the memory population remains small and it is sufficient to probe the occupation of its first two states. The measurement consists in asking two questions: we apply successively two π -pulse flipping the qubit state from ground $|g\rangle$ to excited $|e\rangle$ state when there is exactly 0 (first question) or 1 (second question) in the memory, each immediately followed by a qubit readout (see Fig. 1c and Supplementary Material). For an iteration of the experiment, this protocol yields four possible outcomes: gg , ge , eg , and ee , corresponding to the two measured qubit states, from which we can build an observable $\hat{x}_i = \lambda_{gg} |gg\rangle\langle gg| + \lambda_{ge} |ge\rangle\langle ge| + \lambda_{eg} |eg\rangle\langle eg| + \lambda_{ee} |ee\rangle\langle ee|$, where the coefficients $\vec{\lambda}$ can be chosen at will. We repeat the experiment M times to build the sum $\hat{X} = \sum_{i=1}^M \hat{x}_i$. Owing to the central limit theorem, the error exponent is then [20]

$$\mathcal{E} = \frac{\left(\langle \hat{X}_{\text{yes}} \rangle - \langle \hat{X}_{\text{no}} \rangle \right)^2}{2(\sigma(\hat{X}_{\text{yes}}) + \sigma(\hat{X}_{\text{no}}))^2}, \quad (1)$$

with $\langle \hat{X}_{\text{yes/no}} \rangle$ and $\sigma(\hat{X}_{\text{yes/no}})$ the average and standard deviation of \hat{X} when the target is present or absent. For each value of the signal N_S and noise N_N , we numerically fine tune the coefficients $\vec{\lambda}$ in the chosen observable \hat{x} in order to maximize the error exponent.

Tuning up the quantum radar The optimal exploitation of quantum correlations between probe and idler also requires to finely tune the pump pulse that recombines these modes. In contrast to the pump amplitude, the delay τ_d and phase offset φ between the two pump pulses (see Fig. 1c) can be chosen by operating the radar without added noise ($N_N = 0$), and at the largest signal setting ($N_S \approx 0.1$). With the target present, we measure the average number of photons in the memory after the first ($N_{M,1,\text{yes}}$) and the second pulse ($N_{M,2,\text{yes}}$) (see Supplementary Material). Figure 2a shows the ratio $N_{M,2,\text{yes}}/N_{M,1,\text{yes}}$ as a function of the phase difference between the two pump pulses for a delay $\tau_d = 86$ ns, exhibiting its cosine dependence on φ . For the quantum

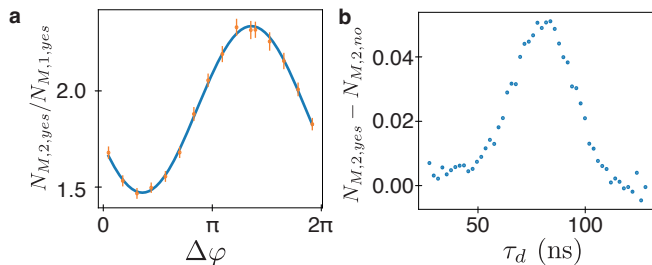


FIG. 2. Tuning up the interferometer. a) Dots: measured average photon number in the memory after the second pump pulse $N_{M,2,yes}$ as a function of the phase difference $\Delta\varphi$ when the target is present, with $N_S \approx 0.1$, and without thermal noise $N_N = 0$. The number is normalized by the measured average number of photons in the memory after the first pump pulse $N_{M,1,yes}$. Line: cosine function fitted to the oscillation with a phase offset $\Delta\varphi_{opt} = 4.385$ b) Dots: measured average photon number change in the memory after the second pump pulse when the target is present or absent as a function of the delay τ_d .

radar experiment, we operate at the maximum of this cosine function. The cosine dependence originates from an interference. In fact, our experiment implements a new kind of SU(1,1) interferometer [32, 38, 39], where one of the arms that host the TMSV is a stationary mode. In this particular case, the asymmetric loss probability κ on one arm prohibits witnessing any remaining entanglement. At this optimal φ , we optimize τ_d by measuring the average number of photons in the memory after the second pulse with ($N_{M,2,yes}$) and without ($N_{M,2,no}$) the target. The population in the memory is maximum for $\tau_{d,opt} \approx 86$ ns, see Fig. 2b.

The last parameter we vary to tune the joint measurement is the amplitude of the second pump, which can be recast as a gain G of the second two-mode squeezing operation. There is no known closed form for the optimal gain G for a given set of N_S , N_N and κ , in particular if the photo-counting errors are factored in. We set N_S and N_N to particular values and measure the error exponent \mathcal{E} for several values of G . For the settings of Fig. 3, it reaches a maximum $\mathcal{E} = 2.9(2) \cdot 10^{-5}$ for a gain of about $G \approx 1.015$. The amplification and the error exponents are very small but it is precisely the regime where a quantum advantage is expected [20]. The corresponding choice of measured observable is shown in the inset of Fig. 3 for that maximum.

Quantum advantage and inherent limitations In order to compute the quantum advantage $Q = \mathcal{E}/\mathcal{E}_{cl}$, we now need to carefully calibrate the three parameters that set \mathcal{E}_{cl} : the signal photon number N_S , the injected noise photon number N_N and target reflectivity κ . Each parameter is determined during the same experimental run, using a dedicated protocol.

The signal photon number is set by the first squeezing operation, in which the circuit acts as a phase-preserving amplifier of gain G_0 , giving $N_S = G_0 n_{th}^b + (G_0 - 1)(1 + n_{th}^m)$ with n_{th}^b and n_{th}^m the initial thermal

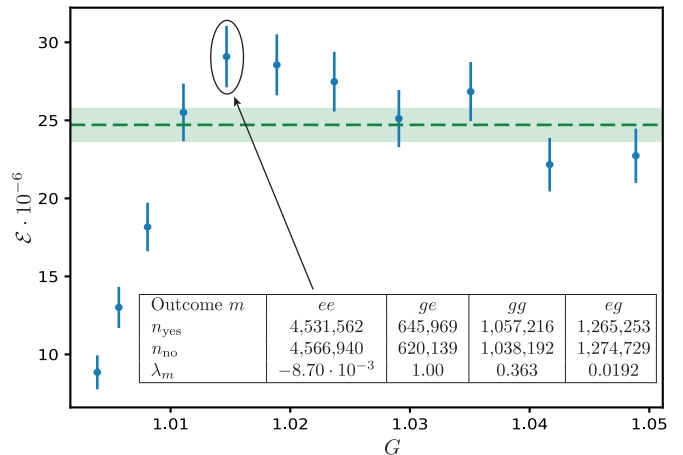


FIG. 3. Observation of a quantum advantage for a microwave radar. Dots: measured error exponent of the quantum radar Eq. (1) as a function of the gain G of the squeezing operation involved in the joint measurement of signal and idler. Here, the number of signal and noise photons are independently measured to be $N_S = 3.53(4) \cdot 10^{-2}$ and $N_N = 10.8(3)$. Each point is obtained using 15 series of $5 \cdot 10^5$ tries. After each series, N_N and N_S are re-calibrated. Green dashed line: quantum Chernoff bound providing the upper bound on the error exponent of any classical radar under the same conditions. The error bars and the colored area represent the uncertainties (see Supplementary Material). Inset: raw measurements for the highlighted point. For each possible outcome m , the table shows the number of occurrences where m is found with the target being present (n_{yes}) or not (n_{no}). The observable \hat{x} that is used to reach the highest error exponent is described by the four λ coefficients. At this point, the quantum advantage is $Q = 1.2(1)$.

populations of the buffer and memory resonators. The pump amplitude tunes the gain to small values $G_0 \gtrsim 1$ to ensure $N_S \ll 1$. To characterize N_S , we make use of the fact that the first squeezing operation creates a photon number for the idler of $N_I = N_S - n_{th}^b + n_{th}^m$. Determining N_S thus only requires to calibrate the initial thermal population of both buffer and memory and measure N_I (see Supplementary Material). Without any active cooling, the thermal equilibrium population of the memory is about $1.5 \cdot 10^{-2}$. We further improve the purity of the TMSV state by initiating all the experimental realizations with sideband cooling of the memory down to $n_{th}^m = 2.5(5) \cdot 10^{-3}$, corresponding to a temperature of 29(1) mK. We also measure an upper bound on n_{th}^b of $5 \cdot 10^{-3}$, which contributes to the error bars in Fig. 3.

To characterize N_N , we use the fact that when pumped at $\omega_\Delta = \omega_b - \omega_m$ with a large enough amplitude, the JRM induces a beam-splitter interaction between the memory and buffer which equilibrates the thermal fluctuations of the two modes. We thus use the qubit to perform a steady-state measurement of the thermal population in the memory when noise and beam-splitter pump are injected to obtain N_N (see Supplementary Material).

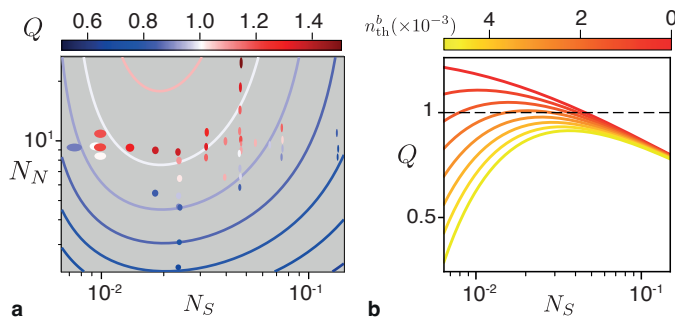


FIG. 4. Quantum advantage sensitivity to parameters. a) Contour plot of the predicted quantum advantage Q as a function of the signal and noise photon numbers N_S and N_N . The model (see Supplementary Material) is an extended version of Ref. [20] with a simplified model of photocounting. The superimposed colored dots represent the measured quantum advantage Q as a function of signal and noise photon numbers N_S and N_N . For each dot, we have measured the quantum advantage Q as a function of receiver gain G and only show its maximum value. The uncertainty on Q is not shown but ranges from $4 \cdot 10^{-2}$ to 0.2. The dots' width and height represent the 4σ uncertainties on N_S and N_N . The initial thermal population in the buffer resonator n_{th}^b is set to $2 \cdot 10^{-3}$. b) Predicted quantum advantage as a function of the signal photon number N_S for a fixed value of noise $N_N = 10$ for various buffer thermal populations ranging from 0 to $5 \cdot 10^{-3}$.

To precisely measure the target reflectivity κ , we use the superconducting device as a quantum vector network analyzer at the signal frequency. We send a coherent state via the auxiliary input line on the buffer that is either directly captured into the memory mode [27–29] by using a pump at ω_Δ or captured only after it reflected off the buffer, went through the target and came back into the buffer. The reflectivity is given by the ratio of the average amplitudes of the states captured into the memory, which we characterize by performing a Wigner tomography of the memory mode (see Supplementary Material). We find $\kappa = 3.02(8) \cdot 10^{-2}$ ($3.2(9) \cdot 10^{-4}$) when the target is present (or not).

In Fig. 3, the measurements of $N_S = 3.53(4) \cdot 10^{-2}$, $N_N = 10.8(3)$ and $\kappa = 3.02(8) \cdot 10^{-2}$ enable us to compute the upper bound on the error exponent that can be reached using coherent illumination: $\mathcal{E}_{\text{cl}} = 2.1(1) \cdot 10^{-5}$. This quantum radar thus beats the best possible classical one by a factor $Q = 1.2(1)$. Note that taking into account the non-zero reflectivity when the target is absent would only lead to a slightly better quantum advantage since \mathcal{E}_{cl} would decrease by about 1%.

The quantum advantage we observe is obtained for a small signal photon number N_S and a large noise photon number N_N . In order to determine the domain in the N_S , N_N parameter space where a quantum advantage can be observed, we reproduce this measurement for various values of N_S and N_N and identify the maximal quantum advantage Q as a function of receiver gain G , with the results shown in Figure 4a. As these measure-

ments and their associated calibrations take at least few hours per point, we explore only a subset of the parameter space. Besides, the error exponent $\mathcal{E}_{\text{cl}} = \kappa N_S / N_N$ gets smaller and smaller as N_N increases or N_S decreases so that it requires a longer measurement time. From this measurement it appears that the quantum advantage increases with N_N as expected. Guha and Erkmen [20] also predict that Q increases at low N_S until reaching its maximum values of $Q = 2$. In our experiment we rather observe that Q diminishes when N_S becomes too small.

We find that this behavior originates from the nonzero initial thermal occupation n_{th}^b and n_{th}^m of the signal and idler modes respectively. A model (see Supplementary Material) taking n_{th}^b and n_{th}^m into account and using an idealized version of our photon-counting measurement is shown in Figure 4a and qualitatively reproduces the experimental results in Fig. 4a. However we note that the model systematically underestimates the measured quantum advantage. While the origin of this discrepancy remains an open question, the modeling of the measurement of observable \hat{x} could be a likely culprit. Note that for this figure, we set n_{th}^b to be $2 \cdot 10^{-3}$ which qualitatively reproduces our result better than the most pessimistic value of $5 \cdot 10^{-3}$ used in Fig. 3 to demonstrate a quantum advantage. On Fig. 4b, we evaluate this model for different values of n_{th}^b , and reveal how the window of signal photon number that exhibit a quantum advantage $Q > 1$ first shrinks then disappears as n_{th}^b increases. We thus find that this thermal population is a major limitation in our experiment, contrary to idler loss [7]. In our case, the latter only lowers the error exponent by $1 - e^{-\gamma_m \tau_d} \approx 2\%$.

Conclusion In conclusion, we have demonstrated an advantage of quantum radar versus classical radar in the microwave domain. The experiment reveals the crucial importance of the purity of the TMSV state used to illuminate the target. Beyond the loss of idler photons, this limitation imposes a stringent upper bound on the idler temperature. The experiment makes clear that using this quantum advantage in practical settings is a tremendous challenge. Strategies that perform independent measurements of signal and idler at room temperature and use post-processing to extract correlations between the two [12, 14] cannot show a quantum advantage $Q > 1$ [4]. Our work highlights what is required to implement such a measurement apparatus. While it is thus difficult to envision a possible future for applications in quantum radar [15–17, 40], the origin of this quantum advantage is still a fascinating puzzle [4, 41–43]. As the experiment confirms, quantum radar provides an oddity in quantum technologies since the quantum advantage increases with added noise. In another context, it is interesting to recast the quantum radar as the signaling of a bit of information (target present or not) through a noisy communication channel beyond the classical Shannon limit [44].

Acknowledgments

This work is part of Quantum Flagship project QMICS that has received funding from the European Union's Horizon 2020 research and innovation program under grant agreement No 820505. We acknowledge IARPA and Lincoln Labs for providing a Josephson Traveling-Wave Parametric Amplifier. The devices were fabricated in the cleanrooms of ENS de Lyon, Collège de France, ENS Paris, CEA Saclay, and Observatoire de Paris. We thank Mikel Sanz, Mateo Casariego, Joonas Govenius, Jeff Shapiro, Pierre Rouchon and Daniel Estève for fruit-

ful discussions.

Author contributions

R.A. performed the experiment and analysed the data. R.D. provided additional support for the experiment and analysis. T.P. fabricated the superconducting circuit and R.A. fabricated the target. R.A., R.D., A.B. and B.H. designed the experiment. B.H. supervised the project. All authors wrote the manuscript.

SUPPLEMENTARY MATERIAL

A. Measurement setup and samples

The cryogenic microwave setup is shown in Fig. 5. The superconducting device in the Cryoperm shield is the exact same device that was used in the experiments of Refs. [27–29]. The 12 m delay line is made of two microwave cables in series. They are made of a 3.58mm semi-rigid coaxial cable constructed with silver plated copper clad steel inner conductor, solid PTFE dielectric and tinned aluminum outer conductor. At the output of the buffer port, and right beyond the directional coupler that injects the pump and noise into the buffer port on demand, a tee with two bandpass filters routes the probe signal at $\omega_b \approx 10.2$ GHz towards the target while it routes the reflected pump at $\omega_p \approx 14$ GHz into a termination load. The spying line was not used during the experiment.

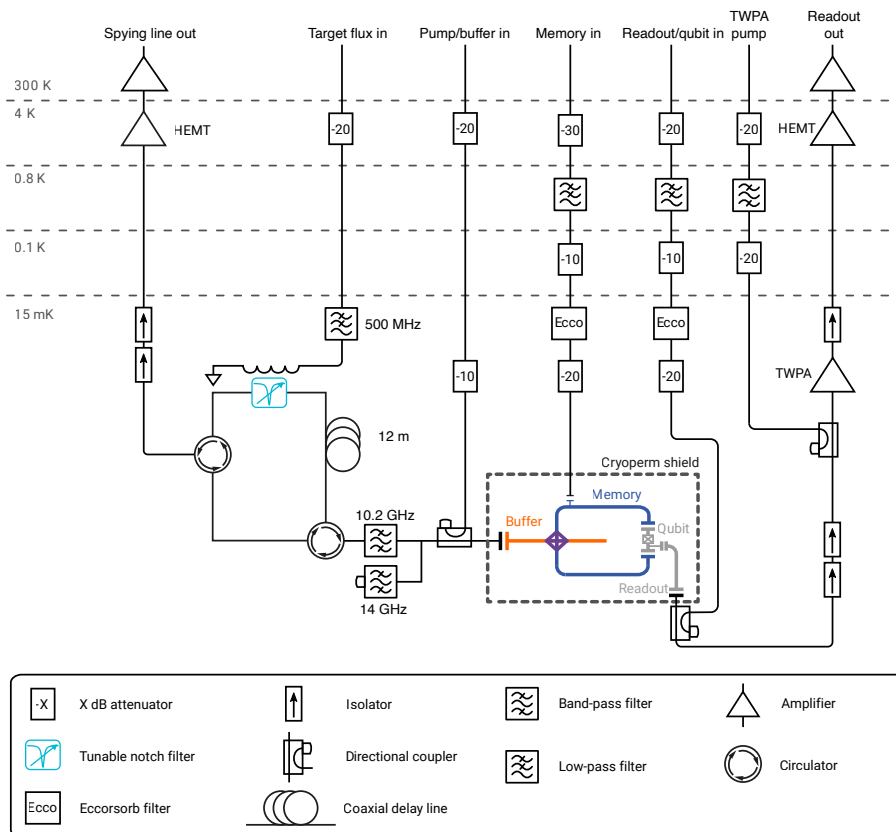


FIG. 5. Schematic of the wiring inside the Bluefors LD250 dilution refrigerator used for the experiment with a base temperature at 15 mK. The Josephson Traveling Wave Parametric Amplifier (TWPA) was graciously provided by the Lincoln Lab.

A key component of the target is realized by a tunable notch filter. It is a stub filter made of a superconducting $\lambda/2$ resonator that shorts the transmission line to ground when on resonance with the signal (Fig. 6a). The tunability comes from the two Josephson junctions in a loop (SQUID) that terminate the resonator. This device is made of sputtered Tantalum on a sapphire chip while the Josephson junctions and the loop are made using e-beam evaporated Al/AlO_x/Al. A flux line is able to flux bias the loop fast enough so that one out of two measurements is performed in the present or absent configuration.

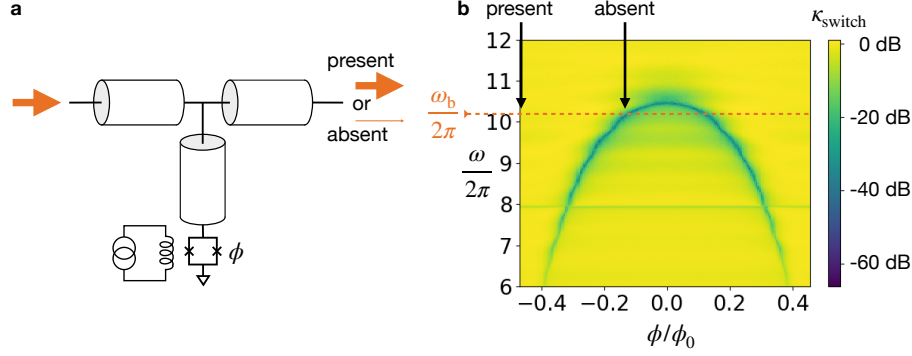


FIG. 6. a. Schematics of the tunable notch filter. b. Measured power ratio between output and input power transmitted through the filter as a function of flux bias ϕ and signal frequency ω . A dashed line indicates the buffer frequency that sets the probe signal frequency in the quantum radar experiment.

Before being placed in the final setup described in Fig. 5, the tunable filter part of the target was tested in a separate dilution refrigerator and its transmission was measured as a function of the current applied through the flux line. In Fig. 6b is shown the measured transmission κ_{switch} (ratio of output and input powers) as a function of signal frequency and flux threading the loop. We measure a 3-dB rejection bandwidth of around 100 MHz, an isolation of around 20 dB and a tunability of the central frequency over several GHz. In the experiment, circulators ensure that the signal that gets out of the buffer port first reaches the tunable notch filter and only comes back through the delay line if the target is present.

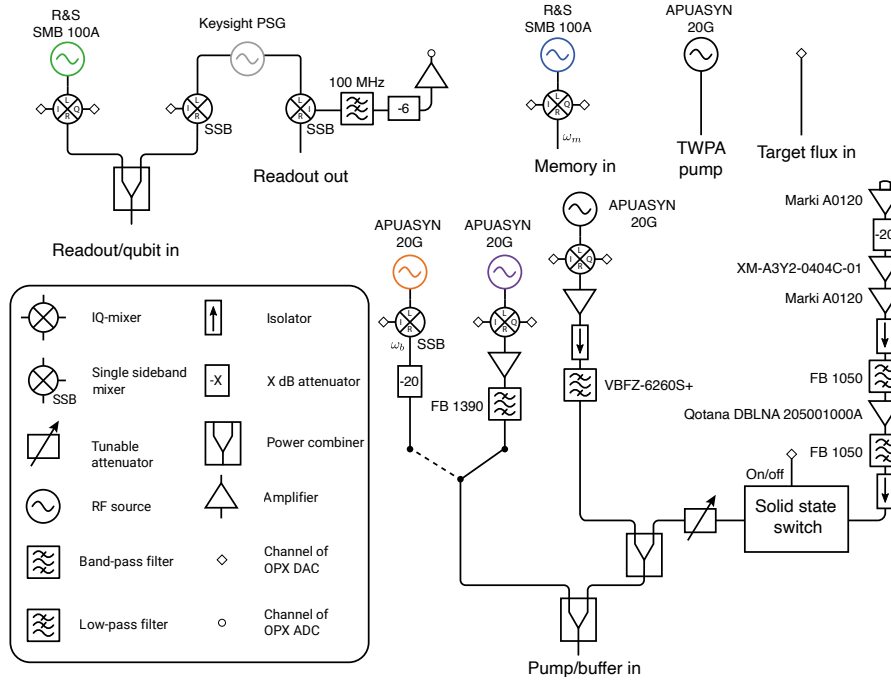


FIG. 7. Schematic of the control electronics. The experiment is controlled by an OPX from Quantum Machines. P/N:DBLNA205001000A

B. Memory mode photo-counting

To count the photon number in the memory (N_M or N_I depending on context), we use the dispersive interaction $-\chi m^\dagger m |e\rangle\langle e|$ with strength $\chi/2\pi = 4.75$ MHz between the memory and the transmon qubit, whose resonance frequency is 4.23 GHz. The qubit lifetime $T_1 = 6.5 \mu\text{s}$ and coherence time $T_2 = 12 \mu\text{s}$ put it in the photon-number resolved regime [45]. In the experiment, we use three different ways to perform the photocounting of the memory mode. The first one is detailed in Fig. 1c. The others are detailed below.

To measure N_I when it is not larger than 2, we use a technique based on Ramsey interferometry explained in Ref [28]. It consists in performing a $\pi/2$ pulse on the qubit, waiting a varying amount of time t , sending another $\pi/2$ pulse and finally measuring the qubit using homodyne detection $s_+(t)$ of the readout resonator output. In order to avoid experimental drifts in gain and phase, we interleave this measurement with another one where the second $\pi/2$ pulse is a $-\pi/2$ pulse, which gives a measurement record $s_-(t)$. We then compute $s(t) = s_+(t) - s_-(t)$. A typical measurement is shown in Fig. 8. Because of the dispersive coupling between the memory and the qubit, we observe oscillations of the readout record $s(t)$. Finally, we can fit those oscillations $s(t)$. Assuming that the memory is in a thermal state, and for $t \ll T_2$ or $N_I \ll 1$, we find

$$s(t) \propto e^{-t/T_2} \sum_{k=0}^{\infty} \frac{N_I^k}{(N_I + 1)^{k+1}} \cos(t(\chi k + \beta k^2)), \quad (2)$$

with $\beta/(2\pi) = 70$ kHz the next higher order non-linear term $-\beta(m^\dagger m)^2 |e\rangle\langle e|$ in the Hamiltonian and $T_2 = 12 \mu\text{s}$ the qubit decoherence time. The factors $\frac{N_I^k}{(N_I + 1)^{k+1}}$ are the probability to find k photons in a thermal state with average photon number N_I .

When N_I is larger, we use another method based on measuring the resonator relaxation towards its equilibrium population by monitoring the probability of having exactly 0 photons in the resonator. To measure this probability, we use a long π -pulse on the qubit that is selective on the presence of 0 photons in the cavity and then repeatedly measure the qubit population $P_e(t)$ for various waiting times t between the initialization of the memory and the photon number selective π -pulse. By assuming that the memory is initially in a thermal state with average photon number N_I , we find that

$$P_e(t) = \frac{1}{N_I e^{-t/T_1} + (1 - e^{-t/T_1}) n_{\text{th}}^m + 1} \approx \frac{1}{N_I e^{-t/T_1} + 1}, \quad (3)$$

with $T_1 = 4.1 \mu\text{s}$ the relaxation time of the memory. We can then fit the measured qubit excitation to this equation to find the average photon number initially contained in the memory.

1. Calibration of n_{th}^m

Using the Ramsey interferometry technique described above, we measured a thermal equilibrium population of $1.5(1) \cdot 10^{-2}$ for the memory mode, which corresponds to an approximate temperature of 41 mK. To improve the performance of the radar, we actively cool down the memory using a beam-splitter interaction between the memory and a higher frequency mode activated by pumping at the difference of the two frequencies. Since this other mode has a much lower quality factor than the memory and the beam-splitter interactions tends to even the number of photons, we are able to cool the cavity down to $n_{\text{th}}^m = 2.5(5) \cdot 10^{-3}$. By chance, this cooling transition is merely 79 MHz above of the two-mode squeezing transition enabling us to use the same mixer and lines for initial cooling and radar operation. All of the error exponent measurements we present are preceded by this 1.2 μs long cooling pulse.

2. Calibration of N_S

The calibration of the signal photon number N_S is realized by measuring the average number of photons N_I in the memory right after the first two-mode squeezing operation. The two are related by $N_I - n_{\text{th}}^m = N_S - n_{\text{th}}^b$.

Finally to convert this average number of idler photons N_I into an average number of signal photons N_S we need to know the difference between the thermal populations of buffer and memory and while we were able to measure the thermal population of the memory with a relatively good precision to $n_{\text{th}}^m = 2.5(5) \cdot 10^{-3}$, we were only able to place an upper bound of $5 \cdot 10^{-3}$ on the number of thermal photons of the buffer using a technique similar to the one described in Section B3.

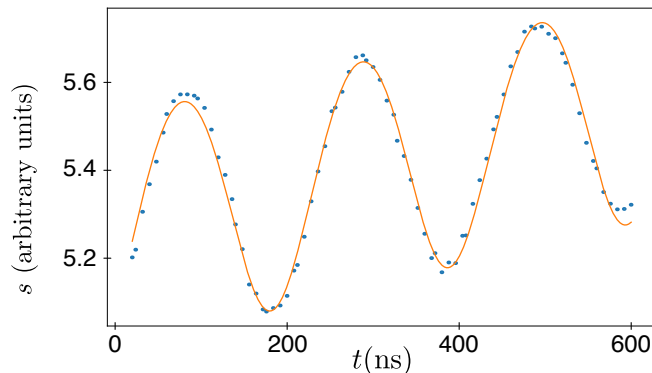


FIG. 8. Typical result of an average signal measurement sequence using the Ramsey interferometry technique right after the first two-mode squeezing operation of the radar sequence. Dots: measured signal s . Solid line: fit of the oscillations using Eq. (2) with $N_I = 0.104(1)$.

We also use this measurement to estimate the receiver gain G . Indeed the number of photons N_I we measure after a two-mode squeezing operation of gain G is given by $N_I = Gn_{\text{th}}^m + (G - 1)(1 + n_{\text{th}}^b)$ leading to $G = (1 + N_I + n_{\text{th}}^b)/(1 + n_{\text{th}}^m + n_{\text{th}}^b)$.

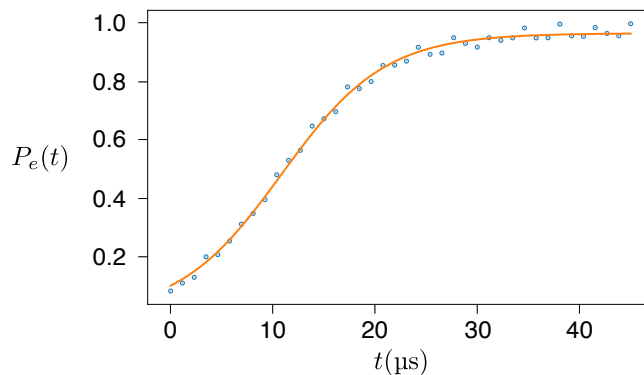


FIG. 9. Typical measurement of the noise photon number N_N using the relaxation method. Dots: excited population of the qubit as a function of waiting time t after the measurement sequence. Solid line: fit of the relaxation Eq. (3) with $N_N = 8.6(5)$.

3. Noise setup and calibration of N_N

As shown in Fig. 7, the noise photons N_N are generated at room temperature by amplifying the Johnson-Nyquist noise of a $50\ \Omega$ resistor using a chain of amplifiers. To avoid saturating the final amplifiers or overloading the cooling capacity of the dilution refrigerator, bandpass filters are used to suppress the noise outside of the buffer frequency window. The filters used are Marki FB 1050 with a 1.5 GHz bandwidth which is much larger than the 20 MHz bandwidth of the buffer making the noise perfectly thermal from the point of view of the buffer. To adjust the noise, an electrically tunable attenuator is used as well as a solid-state switch (HMC-C019) which is able to turn the noise on after the generation of the signal/idler pair but before the signal possibly comes back from the target.

To calibrate the noise in-situ, while the noise is turned on, we first activate the beam-splitter interaction between memory and buffer by pumping the JRM at $\omega_\Delta = \omega_b - \omega_m$ which equalizes the photon number population inside both resonators. Once a steady state is reached, we switch off this pump and measure the average number of photons in the memory N_N using the relaxation method described above.

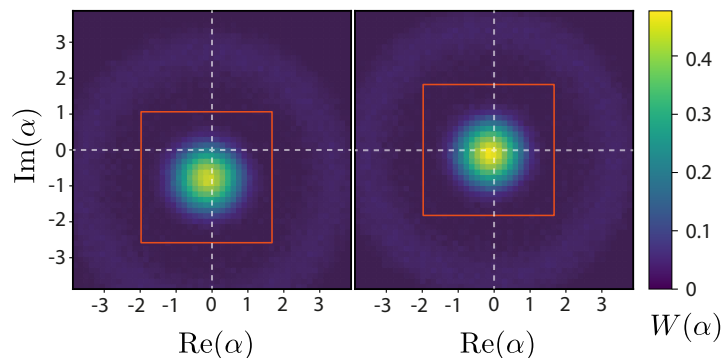


FIG. 10. Typical Wigner tomograms used in the calibration of the target reflectivity κ . The red square delimits the area used to find the average amplitude (see Section C). Left: Measured Wigner function of the memory after a buffer-memory swap performed right after a coherent drive of the buffer mode. Right: Measured Wigner function of the memory after a buffer-memory swap performed after a reflection on the target when present.

C. Calibration of κ

To measure the target reflectivity κ , we implemented a sort of narrow-band vector network analyzer (VNA) using the superconducting circuit as a sensor: first, we send a short coherent pulse (a 28 ns long wavepacket shaped by a hyperbolic secant) through the directional coupler, the wavepacket then enters the buffer where we can choose to either measure it or let it bounce back, through the target and back to the buffer again with the attenuation κ we want to estimate. To measure the average amplitudes of this wavepacket before and after going through the target, we swap the buffer with the memory either before or after the wavepacket goes through the target and then perform a full Wigner tomography of the memory state using the qubit. By taking the average amplitude weighted by the Wigner function, we can find the amplitude α_1 and α_2 of the incident and reflected signals and deduce the target reflectivity $\kappa = \left| \frac{\alpha_2}{\alpha_1} \right|^2$. Note that the results are independent of the swap efficiency since the same swap sequence is used for the incident and reflected waves. We measure $\kappa_{\text{yes}} = 3.02(8) \cdot 10^{-2}$ when the target is nominally present and a residual $\kappa_{\text{no}} = 3.2(9) \cdot 10^{-4}$ when the target is nominally absent which agrees well with our independent 20 dB isolation measurement.

The Wigner tomography is performed by first displacing the memory with an amplitude $-\alpha$ and then measuring its parity using the qubit. These parity measurements consist in applying a fast, unconditional, $\pi/2$ pulse on the qubit followed by a waiting time of π/χ and another $\pi/2$ pulse before reading out the state of the qubit. For additional robustness, we interleave sequences using a final $\pi/2$ pulse with sequences using a final $-\pi/2$ pulse as described in [29]. A large faint ring with a radius of around 3 appears in the Wigner tomograms (see Fig. 10). We attribute it to a breakdown of the dispersive approximation for such large excitations. Since we compute the average amplitude $\langle \alpha \rangle$ using $\langle \alpha \rangle = \int W(\alpha) \alpha d\alpha$, this ring would introduce a bias on the measurement. To eliminate this bias, we truncate the measured Wigner function to a smaller square roughly centered on the average amplitude. This smaller square is represented in red in Fig. 10.

D. Quantum radar model

When the initial state is generated by a squeezing operation with gain G_0 , the signal and idler modes form a gaussian state with a zero mean described by the covariance matrix of the two pairs of creation and annihilation operators $(\hat{a}_S^\dagger, \hat{a}_S)$ and $(\hat{a}_I^\dagger, \hat{a}_I)$: $V_E = \langle (\hat{a}_S^\dagger \hat{a}_I^\dagger \hat{a}_S \hat{a}_I)^\dagger (\hat{a}_S^\dagger \hat{a}_I^\dagger \hat{a}_S \hat{a}_I) \rangle$

$$V_E = \begin{pmatrix} N_S + 1 & 0 & 0 & N_C \\ 0 & N_I + 1 & N_C & 0 \\ 0 & N_C & N_S & 0 \\ N_C & 0 & 0 & N_I \end{pmatrix} \quad (4)$$

with $N_C = \sqrt{G_0(G_0 - 1)(1 + n_{\text{th}}^m + n_{\text{th}}^b)}$, $N_S = G_0 n_{\text{th}}^b + (G_0 - 1)(n_{\text{th}}^m + 1)$ and $N_I = (G_0 - 1)(n_{\text{th}}^b + 1) + G_0 n_{\text{th}}^m$.

The attenuation by the noisy target transforms the operator \hat{a}_S into a reflected $\hat{a}_R = \sqrt{\kappa}\hat{a}_S + \sqrt{1-\kappa}\hat{a}_N$ (when the target is absent, we take $\kappa = \kappa_{\text{no}}$) with \hat{a}_N the operator describing a thermal field with average photon number $\frac{N_N}{1-\kappa}$. Hence at the receiver, the state is still gaussian with zero mean and a covariance matrix

$$V_R = \begin{pmatrix} \kappa N_S + N_N + 1 & 0 & 0 & \sqrt{\kappa} N_C \\ 0 & N_I + 1 & \sqrt{\kappa} N_C & 0 \\ 0 & \sqrt{\kappa} N_C & \kappa N_S + N_N & 0 \\ \sqrt{\kappa} N_C & 0 & 0 & N_I \end{pmatrix}. \quad (5)$$

Finally, after the recombination step between the reflected signal and idler with a two-mode squeezing operation of gain G and at the optimal phase offset $\Delta\varphi_{\text{opt}}$, the state present in the memory is a gaussian state with zero mean and with an annihilation operator $\hat{a}_M = \sqrt{G}\hat{a}_I + \sqrt{G-1}\hat{a}_R^\dagger$. Before being measured, the memory thus contains an average number of photons

$$\langle a_M^\dagger a_M \rangle = GN_I + (G-1)(1 + \kappa N_S + N_N) + 2\sqrt{\kappa G(G-1)}N_C. \quad (6)$$

In the experiment, we perform a measurement that tries to measure the probabilities that mode a_M has 0 or 1 photons. However, finite lifetimes and coherence times of the qubit and memory modes lead to errors in this photocounting. In practice, the quantum advantage is obtained by optimizing the observable \hat{x}_i by tuning the $\vec{\lambda}$ coefficients (see main text). The model simplifies this procedure by assuming a perfect photcounter and truncating the simulated measured outcome to 0, 1 or 2. The latter is chosen if more than 2 photons are found.

E. Uncertainties calculations

The uncertainty on the estimation of the quantum advantage $Q = \frac{\mathcal{E}}{\mathcal{E}_{\text{cl}}}$ comes from two sources: the uncertainties on the estimation of the quantum Chernoff bound for the classical error exponent \mathcal{E}_{cl} and those coming from the measurement of the error exponent \mathcal{E} of the quantum radar.

Let us examine the estimation of the uncertainty of the quantum Chernoff bound \mathcal{E}_{cl} first. The three parameters used in the computation are the target reflectivity κ , the number of photons in the signal beam N_S and the number of noise photons N_N . The measurements of those three parameters are described in Sections B 2, B 3 and C. The uncertainties we used on N_S and N_N come from the non-linear fitting routine which means that they are mostly statistical and do not take into account imperfections in the measurement protocols. To estimate the uncertainty on κ , different probe amplitudes are used and the distribution of results allows us to make sure that κ is independent of power (at least in the low power range we are considering) as well as provide a statistical uncertainty on the value of κ . These three uncertainties are then propagated through the expression of $\mathcal{E}_{\text{cl}} = \frac{\kappa N_S}{4N_N}$ by assuming no correlations between the three quantities which gives a total uncertainty of

$$\Delta\mathcal{E}_{\text{cl}} = \frac{\kappa N_S}{4N_N} \sqrt{\frac{\Delta^2(\kappa)}{\kappa^2} + \frac{\Delta^2(N_S)}{N_S^2} + \frac{\Delta^2(N_N)}{N_N^2}} \quad (7)$$

for \mathcal{E}_{cl} .

For the measured error exponent \mathcal{E} of the quantum radar, the uncertainties on the measured mean and variance of the observable \hat{X} are required. Assuming a large number of repetitions M and a Gaussian distribution for \hat{X} (which is true if M is large enough to fulfill the central limit theorem conditions), the uncertainties on $\langle \hat{X} \rangle$ and $\sigma(\hat{X})$ are given by $\Delta(\langle \hat{X} \rangle) = \sigma(\hat{X})/\sqrt{M}$ and $\Delta(\sigma(\hat{X})) = \sigma(\hat{X})/\sqrt{2M}$. To propagate these uncertainties through Eq. (1) to the uncertainty on \mathcal{E} , we use the two following rules

$$\Delta\left(\frac{X}{Y}\right) = \left|\frac{X}{Y}\right| \sqrt{\left(\frac{\Delta X}{X}\right)^2 + \left(\frac{\Delta Y}{Y}\right)^2 + 2\frac{r(X,Y)\Delta(X)\Delta(Y)}{XY}}$$

$$\Delta(X+Y) = \sqrt{\Delta(X)^2 + \Delta(Y)^2 + 2r(X,Y)\Delta(X)\Delta(Y)}$$

where $r(X,Y) = \frac{\text{Cov}(X,Y)}{\Delta(X)\Delta(Y)}$ is the Pearson correlation coefficient between the stochastic variables X and Y . We therefore require to estimate three Pearson coefficients in the experiment:

1. $r \left[\left(\langle \hat{X}_{\text{yes}} \rangle - \langle \hat{X}_{\text{no}} \rangle \right)^2, (\sigma(\hat{X}_{\text{yes}}) + \sigma(\hat{X}_{\text{no}}))^2 \right]$ between the signal and the noise of the quantum radar. One might expect some positive correlations between the two since both should be affected similarly by technical drifts in the parameters, and one should be proportional to the other. Since estimating those correlations experimentally is quite difficult, we choose to consider the worst case scenario that maximizes the uncertainty on \mathcal{E} and use the value 0 in the calculations .
2. $r \left[\langle \hat{X}_{\text{yes}} \rangle, \langle \hat{X}_{\text{no}} \rangle \right]$ between the measured signals when the target is present and absent. One might expect some systematic biases (such as the value of κ or N_S drifting) to push this coefficient above 0 but we take again the most pessimistic value, which is 0 once again.
3. $r \left[\sigma(\hat{X}_{\text{yes}}), \sigma(\hat{X}_{\text{no}}) \right]$ between the noise level when the target is present and absent. Just like the previous case, one might also expect some positive correlation between the two distributions. Here the most pessimistic assumption is to take this coefficient to be 1 and assume full correlation.

These three assumptions allow us to put a reasonable upper bound on the value of the uncertainty of \mathcal{E}

$$\Delta(\mathcal{E}) = \frac{1}{\sqrt{M}} \left(\frac{\langle \hat{X}_{\text{yes}} \rangle - \langle \hat{X}_{\text{no}} \rangle}{\sigma(\hat{X}_{\text{yes}}) + \sigma(\hat{X}_{\text{no}})} \right)^2 \sqrt{\frac{1}{2} + \frac{\sigma(\hat{X}_{\text{yes}})^2 + \sigma(\hat{X}_{\text{no}})^2}{\left(\langle \hat{X}_{\text{yes}} \rangle - \langle \hat{X}_{\text{no}} \rangle \right)^2}}. \quad (8)$$

-
- [1] E. Knill and R. Laflamme, *Physical Review Letters* **81**, 5672 (1998).
 - [2] A. Datta, A. Shaji, and C. M. Caves, *Physical Review Letters* **100**, 050502 (2008).
 - [3] S. Lloyd, *Science* **321**, 1463 (2008).
 - [4] M. Bradshaw, S. M. Assad, J. Y. Haw, S.-H. Tan, P. K. Lam, and M. Gu, *Phys. Rev. A* **95**, 022333 (2017).
 - [5] Z. Zhang, S. Mouradian, F. N. C. Wong, and J. H. Shapiro, *Physical Review Letters* **114**, 110506 (2015).
 - [6] F. Xu, X. M. Zhang, L. Xu, T. Jiang, M. H. Yung, and L. Zhang, *Physical Review Letters* **127**, 1 (2021).
 - [7] S. Barzanjeh, S. Guha, C. Weedbrook, D. Vitali, J. H. Shapiro, and S. Pirandola, *Physical Review Letters* **114**, 080503 (2015).
 - [8] J. Bourassa and C. M. Wilson, *IEEE Aerospace and Electronic Systems Magazine* **35**, 58 (2020).
 - [9] D. Luong, B. Balaji, C. W. Sandbo Chang, V. M. Ananthapadmanabha Rao, and C. Wilson, in *2018 International Carnahan Conference on Security Technology (ICCST)* (IEEE, 2018) pp. 1–5.
 - [10] D. Luong, C. W. S. Chang, A. M. Vadiraj, A. Damini, C. M. Wilson, and B. Balaji, *IEEE Transactions on Aerospace and Electronic Systems* **56**, 2041 (2020).
 - [11] C. W. S. Chang, A. M. Vadiraj, J. Bourassa, B. Balaji, and C. M. Wilson, *Applied Physics Letters* **114**, 112601 (2019).
 - [12] S. Barzanjeh, S. Pirandola, D. Vitali, and J. M. Fink, *Science Advances* **6**, eabb0451 (2020).
 - [13] P. Livreri, E. Enrico, L. Fasolo, A. Greco, A. Rettaroli, D. Vitali, A. Farina, F. Marchetti, and D. Giacomini, *Physical Review Letters* **126**, 1 (2021).
 - [14] S. M. Hosseiny, M. Norouzi, J. Seyed-Yazdi, and M. H. Ghamat, *Physical Review Letters* **126**, 1 (2022).
 - [15] J. H. Shapiro, *IEEE Aerospace and Electronic Systems Magazine* **35**, 8 (2020).
 - [16] R. Jonsson, R. Di Candia, M. Ankel, A. Ström, and G. Johansson, in *2020 IEEE Radar Conference (RadarConf20)*, Vol. 2020-Septe (IEEE, 2020).
 - [17] G. Sorelli, N. Treps, F. Grosshans, and F. Boust, *IEEE Aerosp Electron Syst Mag* **37**, 68 (2022).
 - [18] K. M. R. Audenaert, J. Calsamiglia, R. Muñoz-Tapia, E. Bagan, L. Masanes, A. Acin, and F. Verstraete, *Physical Review Letters* **98**, 1 (2007).
 - [19] G. De Palma and J. Borregaard, *Phys. Rev. A* **98**, 012101 (2018).
 - [20] S. Guha and B. I. Erkmen, *Phys. Rev. A* **80**, 052310 (2009).
 - [21] S.-H. Tan, B. I. Erkmen, V. Giovannetti, S. Guha, S. Lloyd, L. Maccone, S. Pirandola, and J. H. Shapiro, *Phys. Rev. Lett.* **101**, 253601 (2008).
 - [22] R. Nair and M. Gu, *Optica* **7**, 771 (2020).
 - [23] Q. Zhuang, Z. Zhang, and J. H. Shapiro, *J. Opt. Soc. Am. B* **34**, 1567 (2017).
 - [24] H. Shi, B. Zhang, and Q. Zhuang, (2022), 10.48550/arXiv.2207.06609.
 - [25] J. Calsamiglia, J. I. de Vicente, R. Muñoz-Tapia, and E. Bagan, *Physical Review Letters* **105**, 080504 (2010).
 - [26] M. Sanz, U. Las Heras, J. J. García-Ripoll, E. Solano, and R. Di Candia, *Phys. Rev. Lett.* **118**, 070803 (2017).
 - [27] T. Peronin, D. Marković, Q. Ficheux, and B. Huard, *Physical Review Letters* **124**, 180502 (2020).
 - [28] R. Dassonneville, R. Assouly, T. Peronin, P. Rouchon, and B. Huard, *Phys. Rev. Applied* **14**, 044022 (2020).
 - [29] R. Dassonneville, R. Assouly, T. Peronin, A. A. Clerk, A. Bienfait, and B. Huard, *PRX Quantum* **2**, 020323 (2021).
 - [30] C. Eichler, D. Bozyigit, C. Lang, M. Baur, L. Steffen, J. M. Fink, S. Philipp, and A. Wallraff, *Physical Review Letters* **107**, 113601 (2011).
 - [31] C. M. Wilson, G. Johansson, A. Pourkabirian,

- M. Simoen, J. R. Johansson, T. Duty, F. Nori, and P. Delsing, *Nature* **479**, 376 (2012).
- [32] E. Flurin, N. Roch, F. Mallet, M. H. Devoret, and B. Huard, *Phys. Rev. Lett.* **109**, 1 (2012).
- [33] E. P. Menzel, R. Di Candia, F. Deppe, P. Eder, L. Zhong, M. Ihmig, M. Haerberlein, A. Baust, E. Hoffmann, D. Ballester, K. Inomata, T. Yamamoto, Y. Nakamura, E. Solano, A. Marx, and R. Gross, *Physical Review Letters* **109**, 250502 (2012).
- [34] N. Bergeal, F. Schackert, M. Metcalfe, R. Vijay, V. E. Manucharyan, L. Frunzio, D. E. Prober, R. J. Schoelkopf, S. M. Girvin, and M. H. Devoret, *Nature* **465**, 64 (2010).
- [35] N. Bergeal, R. Vijay, V. E. Manucharyan, I. Siddiqi, R. J. Schoelkopf, S. M. Girvin, and M. H. Devoret, *Nature Physics* **6**, 296 (2010).
- [36] N. Roch, E. Flurin, F. Nguyen, P. Morfin, P. Campagne-Ibarcq, M. H. Devoret, and B. Huard, *Phys. Rev. Lett.* **108**, 147701 (2012).
- [37] E. Flurin, N. Roch, J. D. Pillet, F. Mallet, and B. Huard, *Phys. Rev. Lett.* **114**, 090503 (2015).
- [38] B. Yurke, S. L. McCall, and J. R. Klauder, *Physical Review A* **33**, 4033 (1986).
- [39] Z. Y. Ou and X. Li, *APL Photonics* **5**, 080902 (2020).
- [40] R. Jonsson and M. Ankel, in *2021 IEEE Radar Conference (RadarConf21)* (2021) pp. 1–6.
- [41] C. Weedbrook, S. Pirandola, J. Thompson, V. Vedral, and M. Gu, *New Journal of Physics* **18**, 043027 (2016).
- [42] Y. Jo, T. Jeong, J. Kim, D. Y. Kim, Y. S. Ihn, Z. Kim, and S.-Y. Lee, (2021), 10.48550/arxiv.2103.17006.
- [43] M. H. Yung, F. Meng, X. M. Zhang, and M. J. Zhao, *npj Quantum Information* **6**, 1 (2020).
- [44] C. H. Bennett, P. W. Shor, J. A. Smolin, and A. V. Thapliyal, *IEEE Transactions on Information Theory* **48**, 2637 (2002).
- [45] D. I. Schuster, A. A. Houck, J. A. Schreier, A. Wallraff, J. M. Gambetta, A. Blais, L. Frunzio, J. Majer, B. Johnson, M. H. Devoret, S. M. Girvin, and R. J. Schoelkopf, *Nature* **445**, 515 (2007).